Temperature-tuned Fermi-surface topology and segmentation in noncentrosymmetric superconductors

Madhuparna Karmakar *

Centre for Quantum Science and Technology, Chennai Institute of Technology, Chennai-600037, India and Department of Physics, Indian Institute of Technology, Madras, Chennai-600036, India

(Received 21 September 2022; revised 1 January 2023; accepted 23 January 2023; published 8 February 2023)

We report the first comprehensive microscopic description of the effect of strong correlations and thermal fluctuations on the properties of noncentrosymmetric superconductors in presence of an in-plane Zeeman field. Away from the weak coupling regime the Bardeen-Cooper-Schrieffer theory breaks down and the superconducting transitions are dictated by the pairing field phase fluctuations. Using a nonperturbative numerical technique *viz.* static path approximation, we demonstrate that short-range fluctuating superconducting pair correlations give rise to Fermi-surface segmentation with direction-dependent pair breaking and hot spots for quasiparticle scattering. A fluctuation-driven finite-temperature topological transition of the Fermi surface is realized, characterized by a shift of the corresponding Dirac point from $\mathbf{k} = 0$ to $\mathbf{k} \neq 0$. Our results provide key benchmarks for the thermal scales and regimes of thermal stability of the properties of these systems, which are important for device applications. Our numerical estimates are in fairly good qualitative agreement with the recent differential conductance and quasiparticle interference measurements on $Bi_2Te_3/NbSe_2$ hybrid. A generic theoretical framework for the finite momentum scattering of quasiparticles and the associated spectroscopic features is proposed, which is expected to be applicable to a wide class of superconducting materials.

DOI: 10.1103/PhysRevB.107.064503

I. INTRODUCTION

Noncentrosymmetric superconductors/superfluids (NCS) with spin-orbit coupling (SOC) and their response to Zeeman field have witnessed rapid progress in the past decade [1–20]. Apart from its realization in fermionic and bosonic ultracold atomic gases [21,22], SOC plays the decisive role in solid-state systems such as magnet-superconductor hybrid (MSH) [23], topological insulator-superconductor heterostructures [24], etc. Key experimental observations on these systems include proximity superconductivity [25], Majorana bound states [26], finite momentum quasiparticle scattering and Fermi-surface segmentation [19,24], and more recently superconducting diode effect [27–37].

Literature on the theoretical investigation of NCS have expanded rapidly. Based almost entirely on the mean-field theory (MFT) there is now a consensus on the ground-state physics of the NCS both in the presence and absence of an applied Zeeman field [19,29,32,38–46]. SOC favors finite-momentum Cooper pair formation and is therefore considered to be a natural choice to realize Fulde-Ferell-Larkin-Ovchinnikov (FFLO) superconductivity [47,48]. MFT studies have established that an interplay of strong SOC and in-plane Zeeman field stabilizes a phase modulated helical superconducting order over a large part of the ground-state phase diagram in two and three dimensions [42–46]. An additional out-of-plane Zeeman field applied to such a system gives rise to topological helical superconducting phases with nonzero Chern number and chiral edge states [49,50].

By construction, MFT excludes pairing field fluctuations, which though it is a suitable approximation deep in the Bardeen-Cooper-Schrieffer (BCS) regime, breaks down away from the weak coupling regime where the different energy scales of the system compete and a perturbative approach to the problem ceases to be valid. In the regime of intermediate coupling, superconducting phase fluctuations dictate the thermal behavior of the system and alter the corresponding thermal scales significantly [51]. Fluctuation effects are particularly pertinent for the lower-dimensional [one-dimensional (1D) and 2D] systems, where (quasi-)long-range superconducting correlations are prone to thermal disordering and Fermi-surface nesting plays crucial role.

For centrosymmetric superconductors, in the regime of intermediate coupling MFT has been found to: (i) grossly overestimate the superconducting T_c, (ii) fail to capture the high-temperature regime of preformed pairs, and (iii) can not account for the pseudogap phase [51]. For lattice fermions, based on nonperturbative numerical approaches it was demonstrated that for centrosymmetric superconductors, MFT estimation of the uniform superconducting state T_c exceeds the experimental observation by 4 times. For the population imbalanced FFLO state, this over estimation is by 20% [52]. A recent beyond MFT work on centrosymmetric superconductors demonstrated that in 2D and 3D continuum systems pairing field fluctuations destabilize the FFLO state at $T \neq 0$ [53]. These observations establish the relevance of thermal fluctuations for the low-dimensional superconductors and raises questions on the MFT estimates of their finite-temperature properties.

There are a limited number of works on the effect of pairing field fluctuations in centrosymmetric

*madhuparna.k@gmail.com

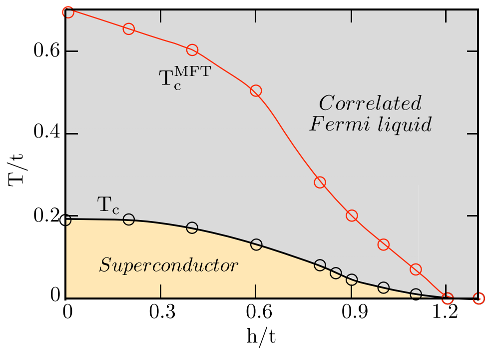

FIG. 1. Comparison of the T_c scales obtained from the mean-field theory (MFT) calculation (top curve) and from the static path approximated (SPA) Monte Carlo technique (bottom curve). MFT leads to the over estimation of the T_c by ~4 times for the uniform and by ~6.5 times for the helical superconducting state. For SPA the T_c is determined using the pairing field structure factor, for the MFT calculation the average pairing field amplitude is tracked as the function of temperature.

superconductors, particularly within the purview of the lattice fermion models, while for the NCS, there are none [2]. Experiments, however, suggest pronounced effect of temperature on the properties of NCS [28,54]. It was recently demonstrated that the performance of superconducting tunnel diode made up of Cu/EuS/Al tunnel junction is robust against thermal fluctuations up to a significantly high operating temperature, a property that makes it appealing for electronic devices [54]. Similarly, magnetotransport measurements on the superconducting state of gated MoS_2 demonstrated that the magnetochiral anisotropy (MA) of this material is strongly dependent on temperature induced superconducting fluctuations and the *ab initio* estimates of the MA parameter shows a discrepancy of five times with respect to (w.r.t.) the experimental results [28]. Such experimental observations call for a deeper theoretical understanding of the effect of thermal fluctuations on the NCS, which at the moment, is lacking. This work attempts to fill this void based on a nonperturbative numerical scheme.

We investigate the 2D NCS in the framework of lattice fermions, using a path integral based Monte Carlo (MC) technique with static path approximation (SPA), in the combined space of competing superconducting interaction (U), SOC (λ), in-plane Zeeman field (h), and temperature (T). Figure 1 encodes one of our key results, wherein we compare the superconducting T_c obtained via SPA to that of the MFT estimate in the h-T plane, for a fixed choice of $U = 4t$ and $\lambda = 0.65t$. In the absence of the Zeeman field ($h = 0$) thermal fluctuation suppresses the T_c by a factor of ~4 compared to the T_c^{MFT}. In the regime of strong Zeeman field ($h \sim t$) this suppression is by a factor of ~6.5.

Having established the regime of thermal stability of the superconducting state in 2D NCS, with accuracy, we next characterized this regime based on the thermodynamic and spectroscopic signatures. Our key results from this work are as follows: (i) the system comprises of Zeeman field tuned quantum critical points (QCP), h_{c1} and h_{c2}, corresponding to a first-order phase transition between the uniform and the helical superconducting phases, and a second-order transition between the helical superconducting and a correlated Fermi liquid (CFL) phase, respectively. (ii) A topological transition of the Fermi surface takes place at $h = h_{tp}$, characterized by a transition between the inter- and intraband paired helical superconducting phases. Across the topological transition the Dirac point shifts from the original $\mathbf{k} = 0$ to $\mathbf{k} \neq 0$. The QCP h_{c1} is not tied to h_{tp} and no symmetry breaking takes place across the topological transition. (iii) In the regime of intermediate h, thermal fluctuations tuned topological transition is realized, driven by the short-range superconducting pair correlations. (iv) Finite momentum scattering of quasiparticles lead to Fermi-surface segmentation in the helical superconducting state. (v) Our results are in qualitative agreement with the experimental observations on $Bi_2Te_3/NbSe_2$ hybrid [24]. The Zeeman field tuned evolution of the in-gap states as observed in the differential conductance measurements, as well as the Fermi-surface segmentation observed via quasiparticle interference (QPI) measurements on $Bi_2Te_3/NbSe_2$ are well captured by our theoretical framework.

The rest of the paper is structured as follows. In Sec. II we discuss the model under consideration for 2D NCS, the numerical technique used to study this system, and the spectroscopic and thermodynamic indicators used to analyze it. We map out the ground-state phases in Sec. III, followed by our analysis of the finite-temperature properties. We discuss the generic formalism for the finite-momentum scattering of quasiparticles in Sec. IV, followed by our conclusions from this work.

II. MODEL, METHOD, AND INDICATORS

Our starting Hamiltonian is the 2D attractive Hubbard model with Rashba spin-orbit coupling (RSOC) and in-plane Zeeman field [42,55,56],

$$\begin{aligned} H = &-t\sum_{\langle ij\rangle,\sigma}(c_{i,\sigma}^{\dagger}c_{j,\sigma} + \text{H.c.}) - \mu\sum_{i,\sigma}\hat{n}_{i,\sigma} - |U|\sum_{i}\hat{n}_{i,\uparrow}\hat{n}_{i,\downarrow} \\ &+ \lambda\sum_{\langle ij\rangle,\sigma\sigma'}(c_{i,\sigma}^{\dagger}(i\hat{\sigma}_y)_{\sigma,\sigma'}c_{j,\sigma'} + c_{i,\sigma}^{\dagger}(-i\hat{\sigma}_x)_{\sigma,\sigma'}c_{j,\sigma'}) \\ &+ h\sum_{i}(c_{i,\uparrow}^{\dagger}c_{i,\downarrow} + c_{i,\downarrow}^{\dagger}c_{i,\uparrow}) \end{aligned} \tag{1}$$

where, $t = 1$ is the hopping amplitude between the nearest neighbors on a square lattice and sets the reference energy scale of the problem, λ is the magnitude of RSOC. $|U| > 0$ is the on-site attractive Hubbard interaction between the fermions, and μ is the global chemical potential, which fixes the electron density. The in-plane Zeeman field (h) is applied along the x axis; $\hat{\sigma}_x$ and $\hat{\sigma}_y$ are the Pauli matrices.

The noninteracting ($U = 0$) energy dispersion of Eq. (1) reads as, $E_{\mathbf{k}}^{\eta} = \xi_{\mathbf{k}} \pm |\lambda g_{\mathbf{k}} + h|$ where, $\xi_{\mathbf{k}} = -2t(\cos k_x + \cos k_y) - \mu$ is the tight binding dispersion for the square lattice. $E_{\mathbf{k}}^{\eta}$ corresponds to the helicity bands labeled by the helicity index $\eta = \pm$. The RSOC is defined as, $g_{\mathbf{k}} = \lambda(-\sin k_y, \sin k_x) = \lambda(-\frac{\partial\xi_{\mathbf{k}}}{\partial k_y}, \frac{\partial\xi_{\mathbf{k}}}{\partial k_x})$. For $h = 0$ the spectra comprises of four dispersion branches and with $h \neq 0$ each branch splits into two [56].

In terms of the Grassmann fields $\psi_{i,\sigma}(\tau)$ and $\bar{\psi}_{i,\sigma}(\tau)$ we write the Hubbard partition function for the interacting ($|U| \neq 0$) Hamiltonian as,

$$Z = \int \mathcal{D}\psi \mathcal{D}\bar{\psi} e^{-S[\psi,\bar{\psi}]} \tag{2}$$

where,

$$\begin{aligned} S = \int_0^\beta d\tau \Bigg[& \sum_{ij,\sigma,\sigma'} \{\bar{\psi}_{i,\sigma}((\partial_\tau - \mu)\delta_{ij} - t_{ij})\psi_{j,\sigma}\} \\ & + \lambda \sum_{\langle ij\rangle,\sigma,\sigma'} (\bar{\psi}_{i,\sigma}(i\hat{\sigma}_y)_{\sigma,\sigma'}\psi_{j,\sigma'} + \bar{\psi}_{i,\sigma}(-i\hat{\sigma}_x)_{\sigma,\sigma'}\psi_{j,\sigma'}) \\ & - |U| \sum_{i,\sigma,\sigma'} \bar{\psi}_{i,\sigma}\psi_{i,\sigma}\bar{\psi}_{i,\sigma'}\psi_{i,\sigma'} + h \sum_{i,\sigma,\sigma'} \bar{\psi}_{i,\sigma}(\hat{\sigma}_x)_{\sigma,\sigma'}\psi_{i,\sigma'} \Bigg]. \end{aligned} \tag{3}$$

The interaction generates a quartic term in ψ, which can not be readily evaluated. In order to make the model numerically tractable we decouple the quartic interaction exactly using Hubbard-Stratonovich decomposition [57,58]. The decomposition introduces the complex scalar bosonic auxiliary fields $\Delta_i(\tau)$ and $\Delta_i^*(\tau)$, which couples to the superconducting pairing. The corresponding partition function reads as,

$$Z = \int \mathcal{D}\Delta\mathcal{D}\Delta^*\mathcal{D}\psi\mathcal{D}\bar{\psi} e^{-S_1[\psi,\bar{\psi},\Delta,\Delta^*]}, \tag{4}$$

where, the action is defined as,

$$\begin{aligned} S_1 = \int_0^\beta d\tau \Bigg[& \sum_{ij,\sigma,\sigma'} \{\bar{\psi}_{i,\sigma}((\partial_\tau - \mu)\delta_{ij}t_{ij})\psi_{j,\sigma}\} \\ & + \lambda \sum_{\langle ij\rangle,\sigma,\sigma'} (\bar{\psi}_{i,\sigma}(i\hat{\sigma}_y)_{\sigma,\sigma'}\psi_{j,\sigma'} + \bar{\psi}_{i,\sigma}(-i\hat{\sigma}_x)_{\sigma,\sigma'}\psi_{j,\sigma'}) \\ & + \sum_i \left(\Delta_i(\tau)\bar{\psi}_{i,\uparrow}\bar{\psi}_{i,\downarrow} + \Delta_i^*(\tau)\psi_{i,\downarrow}\psi_{i,\uparrow} + \frac{|\Delta_i(\tau)|^2}{|U|} \right) \\ & + h \sum_{i,\sigma,\sigma'} \bar{\psi}_{i,\sigma}(\hat{\sigma}_x)_{\sigma,\sigma'}\psi_{i,\sigma'} \Bigg]. \end{aligned} \tag{5}$$

The ψ integral is now quadratic but at the cost of additional integration over $\Delta_i(\tau)$ and $\Delta_i^*(\tau)$. The weight factor for the Δ_i configurations can be determined by integrating out the ψ and $\bar{\psi}$ and using these weighted configurations one goes back and computes the fermionic properties. Formally,

$$Z = \int \mathcal{D}\Delta\mathcal{D}\Delta^* e^{-S_2[\Delta,\Delta^*]}, \tag{6}$$

where,

$$S_2 = \ln[\mathrm{Det}[\mathcal{G}^{-1} - \Delta_i(\tau)]] + \frac{|\Delta_i(\tau)|^2}{|U|}, \tag{7}$$

where, $\mathcal{G}$ is the electron Green's function in the $\{\Delta_i\}$ background. The weight factor for an arbitrary space-time configuration $\Delta_i(\tau)$ involves the determination of the fermionic determinant in that background.

We address this problem using SPA, wherein we treat Δ_i as classical by retaining its complete spatial fluctuations but taking into account only the $\Omega_n = 0$ Matsubara mode in frequency [i.e., $\Delta_i(\tau) \to \Delta_i$] [52,59–61]. The fermions are thus subjected to a static random background of the auxiliary fields.

The effective Hamiltonian reads as,

$$\begin{aligned} H_{eff} = & -t \sum_{\langle ij\rangle,\sigma} (c_{i,\sigma}^\dagger c_{j,\sigma} + \text{H.c.}) - \mu \sum_{i,\sigma} \hat{n}_{i,\sigma} \\ & + \lambda \sum_{\langle ij\rangle,\sigma,\sigma'} (c_{i,\sigma}^\dagger (i\hat{\sigma}_y)_{\sigma,\sigma'} c_{j,\sigma'} + c_{i,\sigma}^\dagger(-i\hat{\sigma}_x)_{\sigma,\sigma'} c_{j,\sigma'}) \\ & + \sum_i (\Delta_i c_{i,\uparrow}^\dagger c_{i,\downarrow}^\dagger + \Delta_i^* c_{i,\downarrow} c_{i,\uparrow}) + \sum_i \frac{|\Delta_i|^2}{|U|} \\ & + h \sum_{i,\sigma,\sigma'} c_{i,\sigma}^\dagger (\hat{\sigma}_x)_{\sigma,\sigma'} c_{i,\sigma'}, \end{aligned} \tag{8}$$

where, $\Delta_i = |\Delta_i|e^{i\theta_i}$ is the complex scalar superconducting pairing field with the pairing field amplitude $|\Delta_i|$ and phase θ_i.

A. Monte Carlo simulation

The random background configurations of $\{\Delta_i\}$ are generated numerically via Monte Carlo (MC) simulation and they obey the Boltzmann distribution,

$$P\{\Delta_i\} \propto \mathrm{Tr}_{c,c^\dagger} e^{-\beta H_{eff}}. \tag{9}$$

For large and random configurations the trace is computed numerically, wherein H_{eff} is diagonalized for each attempted update of Δ_i and converges to the equilibrium configuration via Metropolis algorithm. The process is numerically expensive and involves a computation cost of $O(N^3)$ per update (where $N = L \times L$ is the number of lattice sites), thus the cost per MC sweep is $\sim N^4$. The computation cost is cut down by using a traveling cluster algorithm (TCA), wherein instead of diagonalizing the entire Hamiltonian for each attempted update of Δ_i, we diagonalize a smaller cluster of size $N_c \times N_c$ surrounding the update site [52]. The corresponding computation cost now scales as $O(NN_c^3)$, which is linear in N. This allows us to access larger system sizes with reasonable computation cost. The equilibrium configurations obtained via the combination of MC and Metropolis at different temperatures are used to determine the fermionic correlators [52,59–61].

B. Bogoliubov-de Gennes mean-field theory

Apart from the MC simulation scheme discussed above the ground state of the system is obtained using the alternate scheme of Bogoliubov-de Gennes mean-field theory (BdG-MFT). The corresponding free energy minimization scheme involves optimization over trial solutions w.r.t. $|\Delta_i|$ and $\mathbf{q}$, where $|\Delta_i|$ is real and $\mathbf{q}$ is the pairing wave vector, $|\Delta_\mathbf{q}| = \Delta_0$ corresponds to the amplitude of the uniform superconducting state. For the FFLO phase we choose different trial solutions corresponding to the (i) uniaxial modulation $\Delta_i \propto \Delta_0 \cos(qx_i)$, (ii) 2D modulation $\Delta_i \propto \Delta_0[\cos(qx_i) + \cos(qy_i)]$, and (iii) diagonal modulation $\Delta_i \propto \Delta_0 \cos[q(x_i + y_i)]$. For the helical superconducting phase the trial solution is defined as, $\Delta_i \propto \Delta_0 e^{i\mathbf{q}.\mathbf{r}}$. We work in the grand canonical ensemble over the regime $\mu \in [0 : -4t]$ with $\delta\mu = 0.5t$. The free energy optimization is carried out for different λ and $h \in [0 : 1.5t]$, in each case.

C. Indicators

The various phases of the system are characterized based on the following indicators,

(1) Pairing field structure factor,

$$S(\mathbf{q}) = \frac{1}{N^2}\sum_{ij}\langle \Delta_i \Delta_j^* \rangle e^{i\mathbf{q}.(\mathbf{r}_i - \mathbf{r}_j)}. \tag{10}$$

(2) Single-particle density of states (DOS),

$$N(\omega) = \frac{1}{N}\left\langle \sum_{i,n} \left(\left|u_n^i\right|^2 \delta(\omega - E_n) + \left|v_n^i\right|^2 \delta(\omega + E_n)\right)\right\rangle, \tag{11}$$

where, u_n^i and v_n^i are the BdG eigenvectors corresponding to the eigenvalue E_n.

(3) Spectral function,

$$A(\mathbf{k}, \omega) = -(1/\pi)\text{Im}G(\mathbf{k}, \omega). \tag{12}$$

Here, $G(\mathbf{k}, \omega) = \lim_{\delta\to 0} G(\mathbf{k}, i\omega_n)|_{i\omega_n \to \omega + i\delta}$, with, $G(\mathbf{k}, i\omega_n)$ being the imaginary frequency transform of $\langle c_{\mathbf{k}}(\tau) c_{\mathbf{k}}^\dagger(0)\rangle$.

(4) Low-energy spectral weight distribution at and close to the Fermi level,

$$A(\mathbf{k}, 0) = -(1/\pi)\text{Im}G(\mathbf{k}, 0). \tag{13}$$

(5) Momentum resolved fermionic occupation number,

$$n(\mathbf{k}) = \sum_{\sigma}\langle c_{\mathbf{k},\sigma}^\dagger c_{\mathbf{k},\sigma}\rangle. \tag{14}$$

III. RESULTS

In this section we analyze the ground-state and finite-temperature properties of 2D NCS in terms of the aforementioned indicators. For the MC simulation we work with a lattice size of $L = 24$ and for the BdG-MFT calculations a larger system size of $L = 70$ is used.

A. Fermi-surface evolution with λ and h

We show the RSOC dependence of the Fermi-surface topology in Fig. 2. The columns correspond to selected Zeeman fields, representative of the (i) $\Delta(\mathbf{q} = 0) \neq 0$ uniform superconducting state, (ii) $\Delta(\mathbf{q} \neq 0) \neq 0$ helical superconducting state, and (iii) $\Delta = 0$ CFL state. Each row corresponds to a particular choice of RSOC, for which the Zeeman field is varied. At any RSOC, the $h \leqslant h_{c1}$ regime is trivial and the system comprises of two concentric Fermi surfaces with the Dirac point at $\mathbf{k} = 0$. Increasing RSOC progressively shrinks the inner Fermi surface while enhancing the size of the outer. For $h > h_{c1}$, the helical superconducting state is realized at weak and intermediate RSOC. The Fermi-surface topology is nonmonotonically altered with RSOC in this regime and the Dirac point is shifted to $\mathbf{k} \neq 0$. With increasing RSOC the inner Fermi surface progressively moves

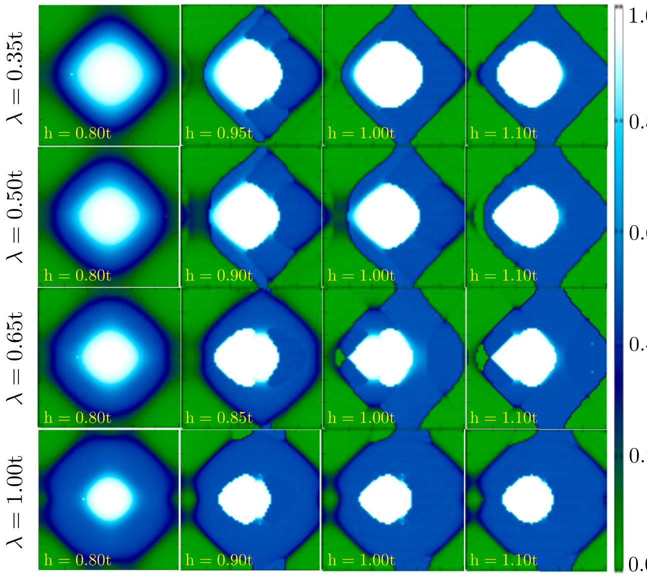

FIG. 2. Evolution of the Fermi surface with in-plane Zeeman field (h) for selected RSOC (λ), presented in terms of the fermionic occupation number $n(\mathbf{k})$ [the color bar corresponds to the magnitude of $n(\mathbf{k})$]. Note the topological transition at intermediate λ-h cross sections, wherein a single self-intersecting Fermi surface is realized. Zeeman effect dominates at strong λ, with significant mismatch in the size of the Fermi surfaces. The calculations are carried out using BdG-MFT for a system size of $L = 70$.

towards the edge of the outer, such that at a critical Zeeman field $h = h_{tp}$ they intersect each other leading to a single self-intersecting Fermi surface, akin to the Limacon of Pascal. The transition from the isolated to the single self-intersecting Fermi surface is topological in nature and the corresponding h_{tp} is tuneable via the combination of the Zeeman field and RSOC. The nature of the superconducting pairing changes from inter- to intraband across this topological transition. The bulk of our results in this paper are at $\lambda = 0.65t$ for which the topological transition between the inter- and intraband pairing takes place at $h_{tp} \sim t$. Over the regime $h_{tp} \leqslant h_{c2}$, the system continues to be in the helical superconducting state but the Fermi surfaces begin to separate out and move apart. For $h > h_{c2}$ the CFL phase is realized.

B. Ground-state phases

We select $\lambda = 0.65t$ as our regime of interest and in Fig. 3 present the corresponding ground-state phase diagram. Figure 3(a) shows the phase diagram in the μ-h plane. The regimes of $\mathbf{q} = 0$ and $\mathbf{q} \neq 0$ pairing are demarcated as the uniform and helical superconducting states, respectively. The low magnetic field regime $h \leqslant h_{c1}$ is a uniform superconducting phase irrespective of the choice of μ. Over the regime $h_{c1} < h < h_{c2}$ a stable helical superconducting phase is realized. The solid curves indicate the μ dependence of h_{c1} and h_{c2}. We next make a particular choice of $\mu = -t$ corresponding to the highest h_{c1} and h_{c2}. The rest of our calculations are carried out at this μ, which corresponds to an electron filling of $n \approx 0.75t$.

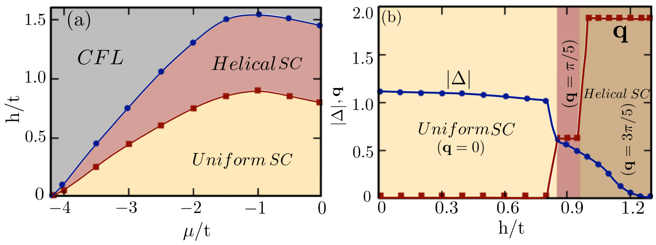

FIG. 3. (a) Ground-state phase diagram in the μ-h plane for the selected RSOC of $\lambda = 0.65t$. The thermodynamic phases include uniform and helical superconducting phases with the corresponding critical fields h_{c1} and h_{c2}, respectively. (b) Zeeman field dependence of average superconducting pairing field amplitude ($|\Delta|$) and pairing momentum ($\mathbf{q}$), at $\lambda = 0.65t$, in the ground state. The first-order transition between the uniform and helical superconducting phases is signaled by the sharp discontinuity in $|\Delta|$ and $\mathbf{q}$. The helical phase comprises of uniaxial modulations with $\mathbf{q} = (0, \pi/5)$ and $(0, 3\pi/5)$.

Figure 3(b) shows the Zeeman field dependence of the mean pairing field amplitude $|\Delta| = \langle|\Delta_i|\rangle$ and the pairing momentum $\mathbf{q}$, at $\lambda = 0.65t$. Over the regime $0 < h \leqslant h_{c1}$, $|\Delta|$ is nearly constant and the corresponding pairing momentum is $\mathbf{q} = 0$. At $h = h_{c1}$ the system undergoes a first-order transition to the helical superconducting state, accompanied by a strong suppression in the pairing field amplitude. Concomitantly, the pairing momentum becomes finite. While $|\Delta|$ undergoes continuous suppression with h, the pairing momenta remains largely constant over the regime $h_{c1} < h \leqslant h_{tp}$. The topological transition between the inter- and intraband helical superconducting states at h_{tp} is accompanied by yet another first-order transition, ascertained by the discontinuity in the pairing momenta $\mathbf{q}$. The jump discontinuity of $\mathbf{q}$ across the topological transition to a single self-intersecting Fermi surface has been recently discussed within the purview of MFT [38].

C. Finite-temperature behavior

We next analyze the finite-temperature behavior of the uniform and helical superconducting phases. The thermodynamic and spectroscopic characterization is obtained in terms of the real space maps, thermal evolution of the Fermi surface and single-particle DOS. The uniform superconducting phase is relatively trivial with quasi-long-range phase correlated uniform superconducting state. We thus mainly focus on characterizing the helical superconducting phase.

1. Spatial maps

We begin by presenting the temperature dependence of the real and momentum space characteristics of the helical superconducting phase. Figure 4 shows the temperature dependence of the superconducting pairing field amplitude ($|\Delta_i|$) (top row) and phase correlation [$\cos(\theta_0 - \theta_i)$] (middle row). The low-temperature helical superconducting phase is characterized by a spatially uniform pairing field amplitude and a 1D modulated phase correlation. Fluctuations progressively destroy the global superconducting order via the loss of (quasi-)long-range phase coherence. The state undergoes spatial fragmentation into phase decohered islands with large

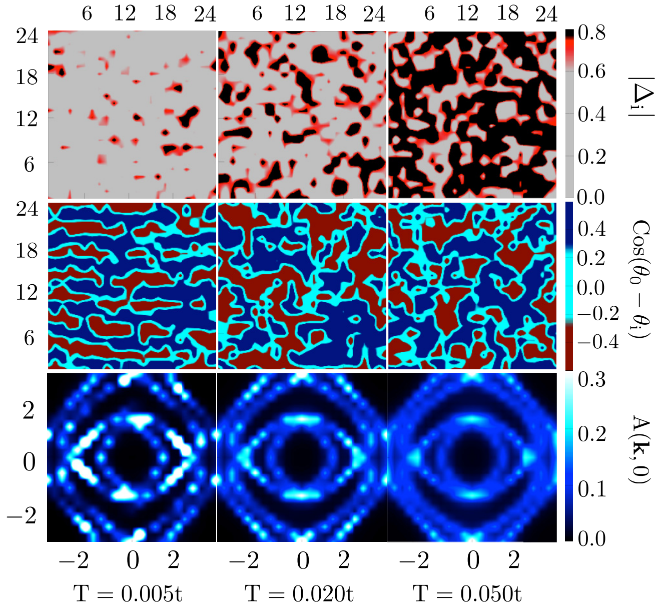

FIG. 4. Real space maps (in the xy plane) corresponding to the superconducting pairing field amplitude, $|\Delta_i|$ (top row) and superconducting phase coherence, $\cos(\theta_0 - \theta_i)$ (middle row), showing the thermal evolution of the helical superconducting state at $h = t$. The bottom row maps out the segmented Fermi surface in terms of the low-energy spectral weight distribution, $A(\mathbf{k}, 0)$ (in the k_xk_y plane). Thermal fluctuations lead to fragmentation of the underlying superconducting state and progressive accumulation of spectral weight at the Fermi level, such that the Fermi-surface isotropy is restored at $T \gtrsim 0.05t$.

local pairing field amplitude, corresponding to a pseudogap phase.

The bottom row of Fig. 4 shows the segmentation of the Fermi surface, mapped out in terms of the low-energy spectral weight distribution $A(\mathbf{k}, 0)$. Finite-q pairing leads to direction-dependent pair breaking, such that only parts of the gapless Fermi surface are available for the scattering of the quasiparticles. Temperature leads to accumulation of spectral weight such that the Fermi-surface isotropy is restored for $T \geqslant 0.05t$. Our results at the low temperatures, shown in Fig. 4 are in fairly good agreement with the experimental observations on $Bi_2Te_3/NbSe_2$ hybrid [24]. QPI measurements on this topological insulator-superconductor hybrid shows Fermi-surface segmentation with q-dependent quasiparticle scattering. The corresponding real space behavior, as established via differential conductance maps show 1D standing wave modulations [24], akin to our results on the superconducting phase coherence shown in Fig. 4.

2. Thermal evolution of the Fermi surface

We next investigate the effect of thermal fluctuations induced short-range superconducting pair correlations. Figure 5 shows the thermal evolution of the Fermi surface at the selected Zeeman field of $h = 0.6t$ and $h = t$. At $h = 0.6t$, the low-temperature phase ($T \leqslant 0.04t$) corresponds to a gapped uniform superconductor, with the Dirac point at $\mathbf{k} = 0$, followed by a gapless superconducting regime, $0.04t < T \leqslant 0.15t$. Within the gapless phase ($0.09t < T \leqslant 0.15t$),

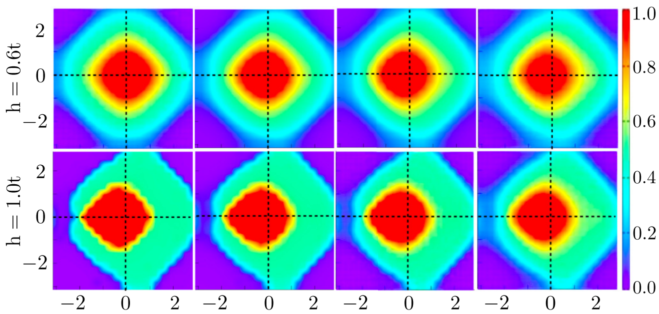

FIG. 5. Temperature dependence of Fermi-surface topology at intermediate ($h = 0.6t$) and strong ($h = t$) Zeeman fields, shown in terms of the fermionic occupation number ($n(\mathbf{k})$). The dashed lines are guide to the eyes for $\mathbf{k} = 0$. Note the self-intersecting Fermi surface at $T = 0.005t$ for $h = t$. The color bar corresponds to the magnitude of $n(\mathbf{k})$.

temperature alters the Fermi-surface topology by progressively shifting the Dirac point from $\mathbf{k} = 0$ to $\mathbf{k} \neq 0$. The change in the Fermi surface at finite temperature arises out of the short-range ($\mathbf{q} \neq 0$) superconducting pair correlations induced by the thermal fluctuations. In the pseudogap regime the Fermi surface undergo fluctuations induced broadening.

At $h = t$, the ground state of the system is in the helical superconducting state with a single self-intersecting Fermi surface over the regime $0 < T \leqslant 0.02t$. Temperature decouples the Fermi surfaces and progressively shifts the inner Fermi surface away from the edge of the outer. The system thus undergoes a temperature-tuned topological transition between the inter- and intraband helical superconducting pair correlations. Loss of local superconducting correlations for $T > 0.04t$ is indicated by the broadening of the Fermi surface.

3. Determination of the thermal scales

The transition temperature (T_c) corresponding to the loss of (quasi-)long-range superconducting phase coherence is determined based on the temperature dependence of the pairing field structure factor [S($\mathbf{q}$)]. We show the same in Fig. 6(a) at different Zeeman fields. The point of divergence of each curve corresponds to the respective T_c. The Zeeman field strongly suppresses the T_c and at $h \sim h_{c1}$ a first-order transition to the helical superconducting phase is realized. Within the helical superconducting phase ($h_{c1} < h \leqslant h_{c2}$) the S($\mathbf{q}$) changes with h via consecutive first-order transitions. The system loses the superconducting order at $h \sim h_{c2}$ via a second-order phase transition, as signaled by the vanishing S($\mathbf{q}$).

In Figs. 6(b)–6(d) we show the h dependence of the single-particle DOS at the Fermi level at three different thermal cross sections. At $T = 0.05t$ [Fig. 6(b)], the system is a gapped uniform superconductor at $h = 0.2t$ with a robust spectral gap at the Fermi level. Increasing h suppresses the gap progressively as observed at $h = 0.4t$ and finally leads to its closure at $h \sim 0.6t$, indicated by a finite spectral weight at the Fermi level. $h = 0.6t$ corresponds to a gapless superconducting state with (quasi-)long-range phase coherence indicated by the broadened but prominent quasiparticle peaks at the gap edges. The system undergoes transition to a regime with helical superconducting correlations at $h \geqslant 0.9t$, characterized by a gapless

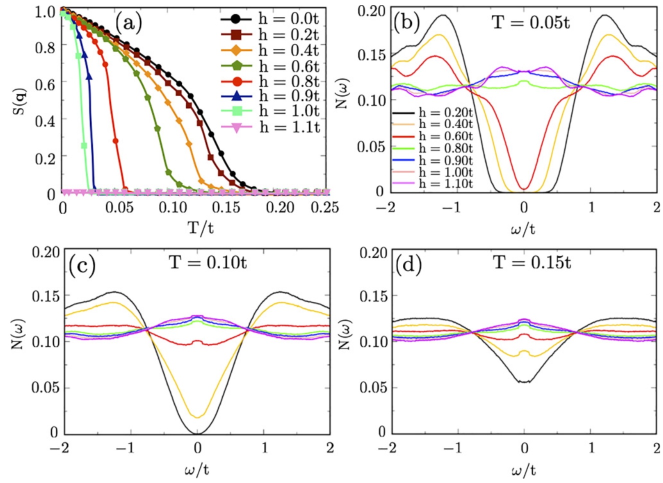

FIG. 6. (a) Temperature dependence of the pairing field structure factor [S($\mathbf{q}$)] at $\lambda = 0.65t$ and different Zeeman fields. The point of divergence of each curve corresponds to the respective T_c. (b)–(d) Zeeman field dependence of the single particle DOS at the Fermi level for the selected temperatures of $T = 0.05t$, $T = 0.10t$, and $T = 0.15t$, respectively.

spectra and thermally diffused signatures of in-gap states. At $h \sim 1.1t$ the spectra is featureless, akin to a magnetic metal.

At $T = 0.10t$ [Fig. 6(c)], the system is a uniform superconductor with suppressed spectral gap at $h = 0.2t$ and a gapless superconductor at $h = 0.4t$. For $h = 0.6t$, a change in the Fermi-surface topology with the shift of the Dirac point to $\mathbf{k} \neq 0$ takes place. The corresponding single-particle DOS shows a sudden large spectral weight accumulation at the Fermi level, which we attribute to the short-range $\mathbf{q} \neq 0$ superconducting correlations. The coherence peaks at the gap edges are strongly suppressed via transfer of spectral weight away from the Fermi level. With further increase in h the system progressively crosses over to the pseudogap phase and eventually to the CFL. The $T = 0.15t$ [Fig. 6(d)] cross section corresponds to a gapless superconductor at low h, which progressively gives way to the pseudogap and then to the CFL phases via spectral weight accumulation at the Fermi level.

The finite-temperature phases are characterized by three thermal scales, T_c, T_g, and T^*, corresponding to the loss of global superconducting phase coherence, collapse of the zero-energy superconducting spectral gap and the crossover between the pseudogap and CFL regimes, respectively. While the T_c is determined based on the temperature dependence of S($\mathbf{q}$), the crossover scales T_g and T^* are determined based on the thermal evolution of $N(\omega)$ at the Fermi level. The high-temperature pseudogap phase is smoothly connected to the CFL via the gradual degradation of the short-range superconducting pair correlations.

4. Thermal phase diagram

We sum up our observations on the finite-temperature behavior of 2D NCS in terms of the thermal phase diagram of the system in the h-T plane, shown in Fig. 7. For our choice of $\lambda = 0.65t$ the QCPs are at $h_{c1} \approx 0.85t$ and $h_{c2} \approx 1.1t$. The thermal scales, T_g, T_c, and T^*, demarcating the gapped and

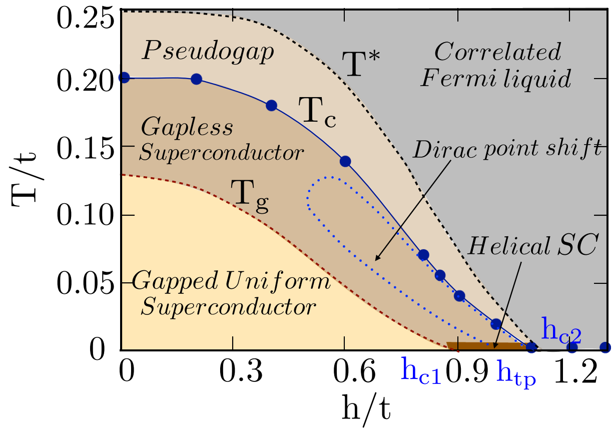

FIG. 7. Thermal phase diagram in the h-T plane at $\lambda = 0.65t$, showing the thermal scales T_c, T_g, and T^*. The finite temperature regime bounded by the dotted curves correspond to the fluctuation induced change in the Fermi-surface topology, characterized by the shift in the Dirac point from $\mathbf{k} = 0$ to $\mathbf{k} \neq 0$. The thermal crossover scales are indicated by the dashed curves and the thermal transition scale is represented by the solid curve with points.

gapless superconducting phases and a pseudogap phase are shown in the figure. The finite-temperature regime enclosed by the dotted curves correspond to the topological helical superconducting phase where the topological transition between the inter- and intraband superconducting pairing is tuned by thermal fluctuations. Fluctuations lead to significant suppression of the thermal scales as compared to the mean-field estimates (see Fig. 1). Our accurate estimates of the thermal scales are expected to serve as benchmarks for the experiments probing the thermal stability of the superconducting states in 2D NCS, which is important for device applications.

D. Comparison with experiment and finite-energy pairing

Within the purview of a lattice fermion model we have established the ground-state and finite-temperature behavior of 2D NCS. Based on a nonperturbative numerical approach we have provided accurate estimates of the thermal scales and the regime of stability of the system against thermal fluctuations. We now compare the spectroscopic properties of the system as obtained via our numerical calculations with the corresponding experimental observations. For the same, in Fig. 8 we compare the Zeeman field dependence of the low-temperature $N(\omega)$ with the differential conductance measurement on $Bi_2Te_3/NbSe_2$ hybrid [24]. In consonance with the experimental observation, the $N(\omega)$ exhibits Zeeman field tuned evolution of the in-gap states. We understand this as follows: owing to the finite-q pairing the $|\mathbf{k}_\uparrow\rangle$ state not just connects with $|-\mathbf{k}_\downarrow\rangle$, but with $|-\mathbf{k}+\mathbf{q}_\downarrow\rangle$ and $|-\mathbf{k}-\mathbf{q}_\downarrow\rangle$ states as well. The resulting dispersion spectra contains multiple branches and gives rise to additional van Hove singularities, which shows up as the in-gap states in $N(\omega)$.

We understand the spectroscopic properties of this system in some detail using Fig. 9 where we show the systematic evolution of the low-temperature spectroscopic indicators of the 2D NCS across the QCPs. At $h = 0$, the RSOC split dispersion spectra contains four branches, as shown via the $A(\mathbf{k}, \omega)$ map. The uniform SC state is interband paired with fermions belonging to the two helicity bands pairing up. The spectra is gapped at the zero energy (Fermi level) [the corresponding $A(\mathbf{k}, 0)$ is featureless] with sharp van Hove singularities at the gap edges, as observed in $N(\omega)$. Zeeman field ($h = 0.6t$) splits the dispersion branches, the spectral gap at the zero energy arising from the uniform interband pairing is suppressed in magnitude. Additional finite-energy shadow gaps open up, which are symmetrically located at $\omega \approx \pm U/2$. These shadow gaps, which are the replicas of the zero-energy gap and recently discussed in the context of Ising superconductors [62], arise out of the intraband pairing in the individual helicity bands. The intermediate ($0 < h \leqslant h_{c1}$) Zeeman field regime thus contains superconducting state with admixture of uniform inter- and intraband pairing. The multiple branches of the dispersion spectra arises out of the interplay between the RSOC and the Zeeman field. The superconducting pairing is between the $|\mathbf{k}_\uparrow\rangle$ and the $|-\mathbf{k}_\downarrow\rangle$ states and there are no Fermi-surface segmentation and in-gap states.

The helical superconducting phase ($h = 0.85t$) with finite-q pairing contains multiple dispersion branches, which

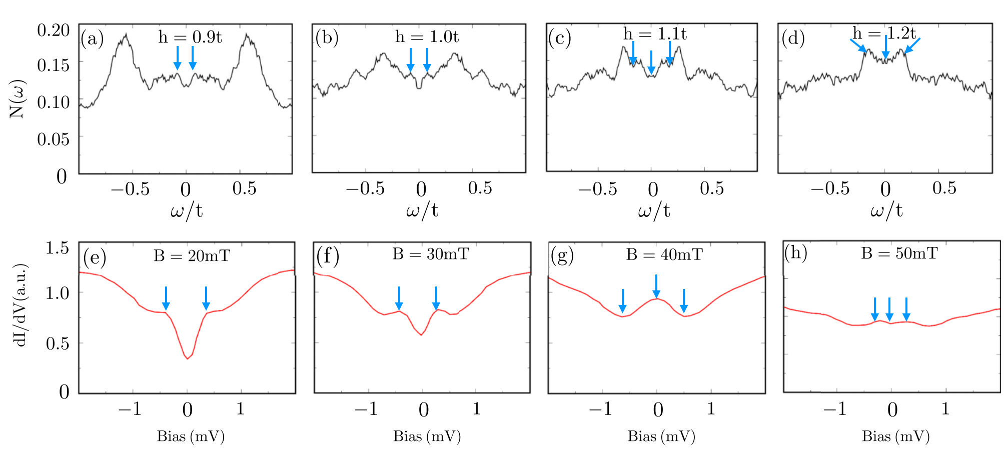

FIG. 8. Comparison of the evolution of the in-gap states with Zeeman field in the helical superconducting phase with the experimental observations on $Bi_2Te_3/NbSe_2$ hybrid [24]. The top panels correspond to the numerically computed single-particle DOS as function of the Zeeman field and the bottom panels show the results obtained via differential conductance measurement on $Bi_2Te_3/NbSe_2$ hybrid, as function of the applied magnetic field $B||\Gamma - M$ [24]. The arrows indicate the in-gap states.

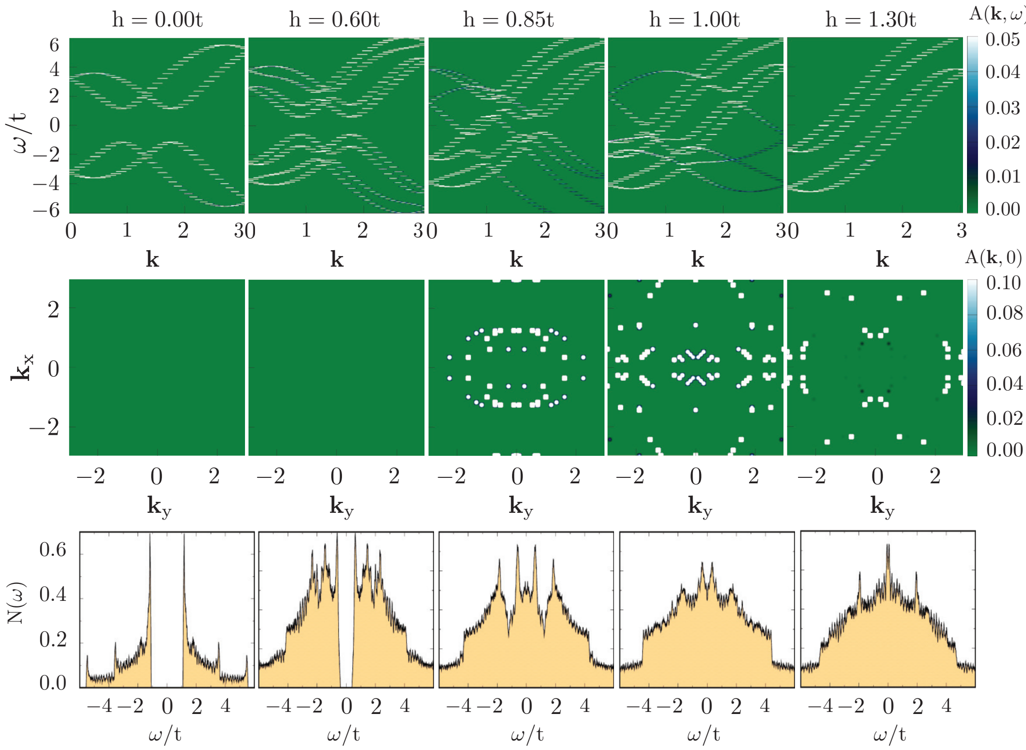

FIG. 9. Spectroscopic properties: (i) spectral function, $A(\mathbf{k}, \omega)$ (top row), (ii) low-energy spectral weight distribution at/close to the Fermi level, $A(\mathbf{k}, 0)$ (middle row), and (iii) single-particle DOS, $N(\omega)$ (bottom row), at the ground state as function of h, determined using BdG-MFT for $L = 70$. For $h = 0$ uniform interband superconductivity is realized between the helicity bands, giving rise to a robust zero-energy superconducting gap. The corresponding $A(\mathbf{k}, 0)$ is featureless and $N(\omega)$ shows prominent gap edge singularities. $h \neq 0$ splits the helicity bands, allows for finite-energy intraband superconducting pairing and opens up symmetrically located shadow gaps. For $h > h_{c1}$ the system is in the helical superconducting state and the multibranched dispersion gives rise to gapless spectra. The corresponding $N(\omega)$ has finite spectral weight at the Fermi level and in-gap states. The Fermi surface is segmented, as observed via $A(\mathbf{k}, 0)$, with isolated hot spots for quasiparticle scattering. The strong h regime ($h > h_{c2}$) corresponds to the correlated Fermi liquid phase with anisotropic Fermi surface akin to a magnetic metal.

connects a larger set of states. Some of these dispersion branches cross the Fermi level, giving rise to the gapless superconductivity. Superconducting pairing is interband in the regime $h_{c1} < h \leqslant h_{tp}$ and the shadow gaps are strongly suppressed. A recent MFT study have discussed the possibility of finite-energy finite-momentum pairing in Fulde-Ferrell superconductors, in the absence of RSOC [63]. The Fermi surface of the helical superconducting state is segmented with direction-dependent pair breaking, as shown via $[A(\mathbf{k}, 0)]$. The crossing of the dispersion branches [as observed in $A(\mathbf{k}, \omega)$] give rise to additional van Hove singularities and the associated in-gap states [see $N(\omega)$]. The self-intersecting Fermi surface realized at $h = h_{tp} = t$ is reflected in $A(\mathbf{k}, \omega)$ as self-intersecting dispersion branches. Superconducting correlations are lost at $h = 1.3t$ and the dispersion spectra is akin to that of a magnetic metal with anisotropic Fermi surface [64].

IV. DISCUSSION AND CONCLUSIONS

Segmentation of the Fermi surface and multibranched dispersion are generic properties associated with finite-q scattering of the quasiparticles. The helical superconducting state constitutes one such example, while the others include FFLO [52,64–73], magnet-superconductor hybrids [23,74,75], magnetic superconductors such as rare-earth quaternary borocarbide (RTBC) [25,64,76–79], etc. Our analysis based on Fig. 9 is generic. Gapless superconducting phase with anisotropic (nodal) Fermi surfaces have been experimentally observed in YNi_2B_2C and $LuNi_2B_2C$ [80–83]. Magnetic fluctuations were proposed to play a key role in defining the Fermi surface and the superconducting gap architecture in these [78] and related class of materials [64,79].

In a similar spirit, nuclear magnetic resonance (NMR) measurements on 2D organic superconductor β''-(BEDT-TTF)$_2$SF$_5$CH$_2$CF$_2$SO$_3$ (BEDT-TTF) showed that the high magnetic field low-temperature regime hosts FFLO state with 1D modulated superconducting order [73]. de Hass-van Alphen measurements and angle-dependent magnetoresistance oscillations were utilized to map out the highly anisotropic 2D Fermi surface of BEDT-TTF [70]. Theoretically, a nonperturbative SPA-based study of the FFLO phase in an isotropic s-wave superconductor have established Fermi-surface segmentation in terms of the corresponding spectroscopic signatures [68]. Thus, irrespective of its origin, finite-q scattering of quasiparticles bring out similar physics in widely different classes of superconducting systems.

In conclusion, based on a nonperturbative numerical approach (*viz.* static path approximation) we have investigated the physics of spin-split two-dimensional noncentrosymmetric superconductors in presence of an in-plane Zeeman field. In the complex parameter space of superconducting interaction, Rashba spin-orbit coupling, Zeeman field, and temperature we have provided the first accurate estimate of the thermal scales and the regime of stability of the superconducting state against fluctuations. We showed that in low-dimensional systems, away from the weak coupling regime the mean-field theory breaks down and leads to gross overestimation of the superconducting phase coherence. Further, we demonstrated finite-temperature topological transition between inter- and intraband paired states, dictated by short-range pairing field fluctuations. The corresponding change in the Fermi surface topology is different from the well-known Lifshitz transition and involves the shifting of the Dirac point from $\mathbf{k} = 0$ to $\mathbf{k} \neq 0$. We further showed that a temperature-controlled Fermi-surface segmentation is realizable in these systems, such that only parts of the Fermi surface serves as hot spots for quasiparticle scattering.

The results presented in this paper provide benchmarks for the thermal scales and the regime of stability of two-dimensional noncentrosymmetric superconductors against thermal fluctuations, which are important from the perspective of device applications. Our results are compared with the experimental observations on $Bi_2Te_3/NbSe_2$ hybrid and are found to be in fairly good qualitative agreement. A generic theoretical framework for finite-momentum scattering of the quasiparticles and the associated Fermi-surface signatures is provided, which should be applicable to a wide class of superconducting materials.

ACKNOWLEDGMENTS

The author acknowledges the use of the high-performance computing cluster facility (AQUA) at IIT Madras, India. Funding from the Center for Quantum Information Theory in Matter and Spacetime, IIT Madras is acknowledged. The author would like to thank Avijit Misra for the critical reading of the manuscript.

[1] R. Meservey and P. Tedrow, Phys. Rep. **238**, 173 (1994).
[2] J. J. Kinnunen, J. E. Baarsma, J.-P. Martikainen, and P. Torma, Rep. Prog. Phys. **81**, 046401 (2018).
[3] L. Fu and C. L. Kane, Phys. Rev. Lett. **100**, 096407 (2008).
[4] J. Alicea, Phys. Rev. B **81**, 125318 (2010).
[5] Y. Oreg, G. Refael, and F. von Oppen, Phys. Rev. Lett. **105**, 177002 (2010).
[6] R. M. Lutchyn, J. D. Sau, and S. Das Sarma, Phys. Rev. Lett. **105**, 077001 (2010).
[7] A. C. Potter and P. A. Lee, Phys. Rev. B **83**, 094525 (2011).
[8] V. Mourik, K. Zuo, S. M. Frolov, S. R. Plissard, E. P. A. M. Bakkers, and L. P. Kouwenhoven, Science **336**, 1003 (2012).
[9] A. Das, Y. Ronen, Y. Most, Y. Oreg, M. Heiblum, and H. Shtrikman, Nature Phys. **8**, 887 (2012).
[10] H.-H. Sun, K.-W. Zhang, L.-H. Hu, C. Li, G.-Y. Wang, H.-Y. Ma, Z.-A. Xu, C.-L. Gao, D.-D. Guan, Y.-Y. Li, C. Liu, D. Qian, Y. Zhou, L. Fu, S.-C. Li, F.-C. Zhang, and J.-F. Jia, Phys. Rev. Lett. **116**, 257003 (2016).
[11] J. M. Lu, O. Zheliuk, I. Leermakers, N. F. Q. Yuan, U. Zeitler, K. T. Law, and J. T. Ye, Science **350**, 1353 (2015).
[12] Y. Saito, Y. Nakamura, M. S. Bahramy, Y. Kohama, J. Ye, Y. Kasahara, Y. Nakagawa, M. Onga, M. Tokunaga, T. Nojima, Y. Yanase, and Y. Iwasa, Nature Phys. **12**, 144 (2016).
[13] X. Xi, Z. Wang, W. Zhao, J.-H. Park, K. T. Law, H. Berger, L. Forró, J. Shan, and K. F. Mak, Nature Phys. **12**, 139 (2016).
[14] B. T. Zhou, N. F. Q. Yuan, H.-L. Jiang, and K. T. Law, Phys. Rev. B **93**, 180501(R) (2016).
[15] L. Fu and E. Berg, Phys. Rev. Lett. **105**, 097001 (2010).
[16] S. Nakosai, Y. Tanaka, and N. Nagaosa, Phys. Rev. Lett. **108**, 147003 (2012).
[17] V. Kozii and L. Fu, Phys. Rev. Lett. **115**, 207002 (2015).
[18] F. Wu and I. Martin, Phys. Rev. B **96**, 144504 (2017).
[19] N. F. Q. Yuan and L. Fu, Phys. Rev. B **97**, 115139 (2018).
[20] M. Alidoust, C. Shen, and I. Žutić, Phys. Rev. B **103**, L060503 (2021).
[21] V. Galitski and I. B. Spielman, Nature (London) **494**, 49 (2013).
[22] J. Dalibard, F. Gerbier, G. Juzeliūnas, and P. Öhberg, Rev. Mod. Phys. **83**, 1523 (2011).
[23] R. Lo Conte, M. Bazarnik, K. Palotás, L. Rózsa, L. Szunyogh, A. Kubetzka, K. von Bergmann, and R. Wiesendanger, Phys. Rev. B **105**, L100406 (2022).
[24] Z. Zhu, M. Papaj, X.-A. Nie, H.-K. Xu, Y.-S. Gu, X. Yang, D. Guan, S. Wang, Y. Li, C. Liu, J. Luo, Z.-A. Xu, H. Zheng, L. Fu, and J.-F. Jia, Science **374**, 1381 (2021).
[25] A. I. Buzdin, Rev. Mod. Phys. **77**, 935 (2005).
[26] M. Z. Hasan and C. L. Kane, Rev. Mod. Phys. **82**, 3045 (2010).
[27] F. Ando, Y. Miyasaka, T. Li, J. Ishizuka, T. Arakawa, Y. Shiota, T. Moriyama, Y. Yanase, and T. Ono, Nature (London) **584**, 373 (2020).
[28] R. Wakatsuki, Y. Saito, S. Hoshino, Y. M. Itahashi, T. Ideue, M. Ezawa, Y. Iwasa, and N. Nagaosa, Sci. Adv. **3**, e1602390 (2017).
[29] A. Daido, Y. Ikeda, and Y. Yanase, Phys. Rev. Lett. **128**, 037001 (2022).
[30] J. J. He, Y. Tanaka, and N. Nagaosa, New J. Phys. **24**, 053014 (2022).
[31] R. Wakatsuki and N. Nagaosa, Phys. Rev. Lett. **121**, 026601 (2018).
[32] N. F. Q. Yuan and L. Fu, Proc. Natl. Acad. Sci. **119**, e2119548119 (2022).
[33] Y. Zhang, Y. Gu, P. Li, J. Hu, and K. Jiang, Phys. Rev. X **12**, 041013 (2022).
[34] M. Alidoust, M. Willatzen, and A.-P. Jauho, Phys. Rev. B **98**, 085414 (2018).
[35] M. Alidoust and H. Hamzehpour, Phys. Rev. B **96**, 165422 (2017).
[36] K. Halterman, M. Alidoust, R. Smith, and S. Starr, Phys. Rev. B **105**, 104508 (2022).
[37] M. Alidoust, Phys. Rev. B **101**, 155123 (2020).
[38] N. F. Q. Yuan and L. Fu, Proc. Natl. Acad. Sci. **118**, e2019063118 (2021).
[39] A. Akbari and P. Thalmeier, Phys. Rev. Res. **4**, 023096 (2022).
[40] P. Thalmeier and A. Akbari, Phys. Rev. B **106**, 064501 (2022).
[41] M. Papaj and L. Fu, Nature Commun. **12**, 577 (2021).
[42] Y. Xu, C. Qu, M. Gong, and C. Zhang, Phys. Rev. A **89**, 013607 (2014).

[43] F. Wu, G.-C. Guo, W. Zhang, and W. Yi, Phys. Rev. A **88**, 043614 (2013).
[44] M. Iskin, Phys. Rev. A **86**, 065601 (2012).
[45] M. Iskin and A. L. Subaşı, Phys. Rev. A **87**, 063627 (2013).
[46] K. Seo, C. Zhang, and S. Tewari, Phys. Rev. A **88**, 063601 (2013).
[47] P. Fulde and R. A. Ferrell, Phys. Rev. **135**, A550 (1964).
[48] A. I. Larkin and Y. N. Ovchinnikov, Zh. Eksp. Teor. Fiz. **47**, 1136 (1964).
[49] W. Zhang and W. Yi, Nature Commun. **4**, 2711 (2013).
[50] Y. Cao, S.-H. Zou, X.-J. Liu, S. Yi, G.-L. Long, and H. Hu, Phys. Rev. Lett. **113**, 115302 (2014).
[51] M. Randeria and E. Taylor, Annu. Rev. Condens. Matter Phys. **5**, 209 (2014).
[52] M. Karmakar and P. Majumdar, Phys. Rev. A **93**, 053609 (2016).
[53] J. Wang, Y. Che, L. Zhang, and Q. Chen, Phys. Rev. B **97**, 134513 (2018).
[54] E. Strambini, M. Spies, N. Ligato, S. Ilić, M. Rouco, C. González-Orellana, M. Ilyn, C. Rogero, F. S. Bergeret, J. S. Moodera, P. Virtanen, T. T. Heikkilä, and F. Giazotto, Nature Commun. **13**, 2431 (2022).
[55] F. Wu, G.-C. Guo, W. Zhang, and W. Yi, Phys. Rev. Lett. **110**, 110401 (2013).
[56] M. Smidman, M. B. Salamon, H. Q. Yuan, and D. F. Agterberg, Rep. Prog. Phys. **80**, 036501 (2017).
[57] J. Hubbard, Phys. Rev. Lett. **3**, 77 (1959).
[58] H. J. Schulz, Phys. Rev. Lett. **65**, 2462 (1990).
[59] M. Karmakar, Phys. Rev. A **97**, 033617 (2018).
[60] M. Karmakar, J. Phys.: Condens. Matter **32**, 405604 (2020).
[61] N. Swain and M. Karmakar, Phys. Rev. Res. **2**, 023136 (2020).
[62] G. Tang, C. Bruder, and W. Belzig, Phys. Rev. Lett. **126**, 237001 (2021).
[63] D. Chakraborty and A. M. Black-Schaffer, Phys. Rev. B **106**, 024511 (2022).
[64] M. Karmakar and P. Majumdar, Phys. Rev. B **93**, 195147 (2016).
[65] T. K. Koponen, T. Paananen, J.-P. Martikainen, and P. Törmä, Phys. Rev. Lett. **99**, 120403 (2007).
[66] M. O. J. Heikkinen, D.-H. Kim, M. Troyer, and P. Törmä, Phys. Rev. Lett. **113**, 185301 (2014).
[67] M. O. J. Heikkinen, D.-H. Kim, and P. Törmä, Phys. Rev. B **87**, 224513 (2013).
[68] M. Karmakar, arXiv:2008.11740.
[69] R. Beyer, B. Bergk, S. Yasin, J. A. Schlueter, and J. Wosnitza, Phys. Rev. Lett. **109**, 027003 (2012).
[70] J. Wosnitza, S. Wanka, J. Qualls, J. Brooks, C. Mielke, N. Harrison, J. Schlueter, J. Williamsd, P. Nixon, R. Winter, and G. Gard, Synth. Met. **103**, 2000 (1999).
[71] J. A. Wright, E. Green, P. Kuhns, A. Reyes, J. Brooks, J. Schlueter, R. Kato, H. Yamamoto, M. Kobayashi, and S. E. Brown, Phys. Rev. Lett. **107**, 087002 (2011).
[72] H. Mayaffre, S. Krämer, M. Horvatić, C. Berthier, K. Miyagawa, K. Kanoda, and V. F. Mitrovic, Nature Phys. **10**, 928 (2014).
[73] G. Koutroulakis, H. Kühne, J. A. Schlueter, J. Wosnitza, and S. E. Brown, Phys. Rev. Lett. **116**, 067003 (2016).
[74] S. Rex, I. V. Gornyi, and A. D. Mirlin, Phys. Rev. B **100**, 064504 (2019).
[75] G. Yang, P. Stano, J. Klinovaja, and D. Loss, Phys. Rev. B **93**, 224505 (2016).
[76] T. Baba, T. Yokoya, S. Tsuda, T. Kiss, T. Shimojima, K. Ishizaka, H. Takeya, K. Hirata, T. Watanabe, M. Nohara, H. Takagi, N. Nakai, K. Machida, T. Togashi, S. Watanabe, X.-Y. Wang, C. T. Chen, and S. Shin, Phys. Rev. Lett. **100**, 017003 (2008).
[77] M. Schneider, G. Fuchs, K.-H. Müller, K. Nenkov, G. Behr, D. Souptel, and S.-L. Drechsler, Phys. Rev. B **80**, 224522 (2009).
[78] H. Kontani, Phys. Rev. B **70**, 054507 (2004).
[79] M. Karmakar and P. Majumdar, arXiv:1808.02012.
[80] E. Boaknin, R. W. Hill, C. Proust, C. Lupien, L. Taillefer, and P. C. Canfield, Phys. Rev. Lett. **87**, 237001 (2001).
[81] T. Watanabe, M. Nohara, T. Hanaguri, and H. Takagi, Phys. Rev. Lett. **92**, 147002(R) (2004).
[82] T. Baba, T. Yokoya, S. Tsuda, T. Watanabe, M. Nohara, H. Takagi, T. Oguchi, and S. Shin, Phys. Rev. B **81**, 180509 (2010).
[83] I.-S. Yang, M. V. Klein, S. L. Cooper, P. C. Canfield, B. K. Cho, and S.-I. Lee, Phys. Rev. B **62**, 1291 (2000).